AGU PUBLICATIONS

Geophysical Research Letters

Supporting Information for

Asymmetrical ocean carbon responses in the tropical Pacific Ocean to La Niña and El Niño

Chaofan Sun[1], Enhui Liao[1]*, Xueming Zhu[2]
[1]School of Oceanography, Shanghai Jiao Tong University, Shanghai, 200030, China
[2]Southern Marine Science and Engineering Guangdong Laboratory (Zhuhai), Zhuhai, 519000, China
*Correspondence to: ehliao@sjtu.edu.cn

Contents of this file

Section S1 Data and model evaluation

We selected chlorophyll, nitrate (NO_3), phosphate (PO_4), sea surface temperature (SST), sea surface salinity (SSS), sea surface height (SSH), and mixed layer depth (MLD) for model evaluation (Figures S3-S7). Among them, the chlorophyll data comes from GlobColour (Maritorena et al., 2010). The NO_3 and PO_4 are from the World Ocean Atlas version 2013 (Garcia, Locarnini, et al., 2013). The SST data is acquired from Optimum Interpolation SST (OISST) v2 (Banzon et al., 2016). The SSS data is obtained from Multi-Mission Optimum Interpolated Sea Surface Salinity Global Dataset (OISSS) v1 (Melnichenko et al., 2021). The SSH data is downloaded from AVISO (Archiving, Validation, and Interpretation of Satellite Oceanographic). The MLD data, based on a density criteria of 0.03 kg/m^3, is from de Boyer Montégut et al. (2004). The observed Niño3.4 index comes from the Earth System Laboratory NOAA (Rayner et al., 2003). The observed mooring data is the tropical atmosphere ocean (TAO) array data, which are downloaded from Pacific Marine Environmental Laboratory NOAA (McPhaden et al., 1998; Sutton et al., 2014).

Model and observation climatological fields are computed from January 1990 to December 2021, except when observations are covered by a shorter period; that is, satellite chlorophyll climatology is computed for 1997–2021, and the observational data of SSS is computed for 2011-2021.

As shown in the SST satellite observation (OISST), the western part of the tropical Pacific Ocean is a warm pool (>28ºC), while the eastern equatorial region (2ºS-2ºN) and the near-shore ocean of South America are occupied by cold water brought by upwelling (Figure S3). During La Niña, there is a low-temperature anomaly (about 1℃) in the tropical Pacific Ocean, while during El Niño, there is a high-temperature anomaly (about 1℃) (Figures S7b, S7d). Our model can capture this spatial distribution feature well, and the magnitude of temperature change as well as the isotherm distribution are basically consistent with observations (Figures S3a-S3b, S7a-S7c). Observation (OISSS) shows a "high-low-high" distribution of salinity in the tropical Pacific Ocean, with an overall range of 33-36.5 psu (Figure S3d). There are two high salinity centers in the southern (10°S-30°S, 150°W-100°W) and northern (15°S-30°S, 175°E-135°W) parts of the tropical Pacific Ocean, and two low salinity centers in the eastern and western near-shore seawaters. The salinity of the southern hemisphere is higher than that of the northern hemisphere in general. The model results can almost catch the main distribution characteristics of salinity, although it is slightly larger than those observations (Figure S3c). This may be associated with the slightly shallower depth of the mixed layer simulated by the model (Figures S3e-S3f), which overestimates the role of precipitation on salinity (Liao et al., 2020). Observation (AVISO) data shows that during La Niña, there is an abnormal decrease in sea surface height (about 0.1m) in the eastern equatorial Pacific Ocean and an abnormal increase (about 0.1m) of sea surface height in the western equatorial Pacific Ocean, while El Niño is reversed (Figures S7f-S7g). Our model can reproduce this sea surface height anomaly (Figures S7e-S7h). These results show that our model has good performance in simulating the circulation dynamics of the tropical Pacific Ocean.

Similarly, we simulate the biological indicators such as nutrient salts (PO_4, NO_3) and chlorophyll (Figure S4). The eastern Pacific Ocean shows high PO_4, high NO_3, and high chlorophyll, with the highest concentration appearing in the upwelling coastal sea of Peru, while the central and western Pacific Ocean show low PO_4, low NO_3, and low chlorophyll. The model largely reproduces the main characteristics of these biological indicators in the observations, indicating that our model can accurately simulate the biogeochemical processes in the tropical Pacific Ocean.

We select three representative moorings on the equator for the TAO data: the Pacific Ocean warm pool margin (190°E), the central Pacific Ocean (221°E), and the eastern Pacific Ocean (251°E). TAO data shows that sea surface temperature has a 1-3°C decrease during La Niña and a 1-5°C increase during El Niño (Figures S5a-S5c). The magnitudes of these temperature anomalies differ little at the selected western, central, and eastern points, but the anomaly has fluctuated more frequently in the eastern Pacific Ocean. The model can simulate these temperature anomalies successfully in the three TAO stations. During La Niña, the salinity has a small increase (less than 0.5 psu), while a strong decrease (0-1.5 psu) during El Niño. The magnitude of these anomalies is slightly higher in the western Pacific Ocean than in the central and eastern Pacific Ocean (Figures S5d-S5f). The model can capture the main features of the salinity anomaly with a slight bias, which may be related to inaccurate calculation of the depth of the mixing layer.

The eastern equatorial Pacific Ocean is characterized by high sea surface pCO_2 (about 480 μatm), extending westward to 175°E, and the distribution of high pCO_2 tends towards the Southern Hemisphere. When the sea surface pCO_2 is higher than that of the atmosphere, the ocean releases CO_2 to the atmosphere, so the air-sea carbon flux in the eastern near-equatorial Pacific Ocean is higher (about 40 $gC/m^2/yr$). The model can almost simulate the spatial distribution of sea surface pCO_2 and air-sea carbon flux, although it is slightly lower than the results of the inversion datasets (Figures S1-S2, S6). In addition, we compare the observed (SOCAT) and simulated (MOM6-COBALT2 model) ocean pCO_2 in the tropical Pacific Ocean during 1990-2021, and the model performs well on the pCO_2 simulation (Figures S8, S9). TAO observations show that there is an increase in sea surface pCO_2 during La Niña (about 20-30 μatm) and a larger decrease during El Niño (about 40-60 μatm). The ocean pCO_2 anomaly in the eastern Pacific Ocean is larger than that in the central and western Pacific Ocean (Figures S5g-S5i). Model simulation results reproduce this spatial distribution, although the magnitude of the anomaly is slightly lower. This result may be related to the shallower mixing layer simulated in our model, which reduces the upward mixing of high CO_2 water in the subsurface, resulting in lower surface ocean pCO_2 (Liao et al., 2020). What's more, there may also be some bias in the sedimentation process of microorganisms from surface to bottom, resulting in a slightly lower DIC concentration in the subsurface of the model. The MOM6-COBALT2 model has shown good performance in simulating the main spatial and temporal features of temperature, salinity, depth of mixed layer, nutrients, chlorophyll, and other indicators. This suggests a good reproduction of the principal characteristics of ocean circulation dynamics and biogeochemical processes. Notably, the model excels in simulating the intensity and variability of air-sea CO_2 flux and ocean pCO_2. It can well simulate the interannual changes of marine carbon cycle in the tropical Pacific Ocean, and provide a powerful tool for this study of the asymmetrical ocean carbon responses in the tropical Pacific Ocean to La Niña and El Niño. In addition, this simulation was well evaluated and applied to examine the air-sea CO_2 flux variability driven by El Niño in the Pacific Ocean and Indian Ocean Dipole (IOD) in the Indian Ocean. For more detailed configurations and evaluations of the model, readers can refer to Liao et al. (2024); Liao et al. (2020).

Section S2 Model setup

The model was spun up from rest for a period of 81 years by repeating the JRA55-do v1.5 forcing in the year of 1959. The atmospheric xCO_2 global average driving MOM6-COBALT2 is from the Global Carbon Budget project (Friedlingstein et al., 2022). The xCO_2 is a global average derived from monthly Mauna Loa Observatory (MLO) and South Pole Observatory (SPO) station data. For model initialization, temperature, salinity, nutrients (nitrate, phosphate, and silicate), and oxygen are sourced from World Ocean Atlas version 2013 (Garcia, Boyer, et al., 2013; Garcia, Locarnini, et al., 2013; Locarnini et al., 2013; Zweng et al., 2013). The initial dissolved inorganic carbon (DIC) and alkalinity (Alk) are obtained from the GLODAP v2 (Olsen et al., 2016). The initial DIC is corrected for the accumulation of anthropogenic carbon to match the level expected in 1959 using the data-based estimate of ocean anthropogenic carbon content (Khatiwala et al., 2013). Other COBALT tracer initial conditions (e.g., ammonium, calcium carbonate) are taken from a preindustrial GFDL-ESM 2 M-COBALT simulation (Stock et al., 2014).

Section S3 Ocean CO_2 flux and pCO_2 decomposition

The air-sea CO_2 flux (FCO_2) is computed using the following Equation:

$$FCO_2 = k_w \alpha (pCO_{2w} - pCO_{2a}) \quad \text{(S1)}$$

Where k_w is the CO_2 gas transfer coefficient computed by a quadratic wind-speed formulation (Wanninkhof, 2014), α is the CO_2 solubility (Weiss & Price, 1980), pCO_{2a} is the atmospheric partial pressure of CO_2, and pCO_{2w} is the sea surface partial pressure of CO_2. The positive FCO_2 denotes an oceanic outgassing of CO_2.

The traditional decomposition framework links variations in ocean pCO_2 to changes in DIC, Alk, temperature, and salinity using the following linear decomposition (Le Quéré et al., 2000; Takahashi et al., 1993):

$$\Delta pCO_{2w} \approx \frac{\partial pCO_{2w}}{\partial DIC}\Delta DIC + \frac{\partial pCO_{2w}}{\partial Alk}\Delta Alk + \frac{\partial pCO_{2w}}{\partial T}\Delta T + \frac{\partial pCO_{2w}}{\partial S}\Delta S \quad \text{(S2)}$$

We extend this decomposition framework to ocean pCO_2 (pCO_{2w}) mechanism analysis to cover all physical and biological processes. The temporal change in the left-hand and the right-hand sides of Equation S2 can be expressed as Equation S3 (Liao et al., 2020):

$$\frac{\partial pCO_{2w}}{\partial t} \approx \frac{\partial pCO_{2w}}{\partial DIC}\frac{\partial DIC}{\partial t} + \frac{\partial pCO_{2w}}{\partial TALK}\frac{\partial ALK}{\partial t} + \frac{\partial pCO_{2w}}{\partial T}\frac{\partial T}{\partial t} + \frac{\partial pCO_{2w}}{\partial S}\frac{\partial S}{\partial t} \quad \text{(S3)}$$

Among them, temporal changes in DIC, ALK, T, and S are affected by ocean physical transports, biological processes, fresh-water fluxes, and air-sea fluxes, as shown in Equation S4-S7 (Liao et al., 2020) :

$$\frac{\partial DIC}{\partial t} = DIC_H + DIC_V + DIC_{FCO_2} + DIC_{Bio} + DIC_{FW} \quad \text{(S4)}$$

$$\frac{\partial Alk}{\partial t} = Alk_H + Alk_V + Alk_{Bio} + Alk_{FW} \quad \text{(S5)}$$

$$\frac{\partial T}{\partial t} = T_H + T_V + T_Q \quad \text{(S6)}$$

$$\frac{\partial S}{\partial t} = S_H + S_V + S_{FW} \quad \text{(S7)}$$

Where the subscript H represents the change term caused by horizontal transport (meridional and zonal convection and diffusion), the subscript V represents the change term caused by vertical transport (vertical convection and diffusion), the subscript FCO_2 represents the DIC change caused by CO_2 exchange at the air-sea interface, the subscript Bio represents the change term caused by biological effects (photosynthesis, respiration, calcium carbonate dissolution and precipitation, nitrification and denitrification process), the subscript FW represents the change term caused by fresh-water fluxes (evaporation, rainfall), and the subscript Q represents the change term caused by heat fluxes (surface heat radiation). Combine Equation S3-S7 to obtain Equation S8 as follows (Liao et al., 2020):

$$\begin{aligned}\frac{\partial pCO_{2w}}{\partial t} \approx\ & \frac{\partial pCO_{2w}}{\partial DIC}\left(DIC_H + DIC_V + DIC_{FCO_2} + DIC_{Bio} + DIC_{FW}\right) + \\ & \frac{\partial pCO_{2w}}{\partial TALK}(Alk_H + Alk_V + Alk_{Bio} + Alk_{FW}) + \\ & \frac{\partial pCO_{2w}}{\partial T}\left(T_H + T_V + T_Q\right) + \\ & \frac{\partial pCO_{2w}}{\partial S}(S_H + S_V + S_{FW})\end{aligned} \quad \text{(S8)}$$

We rearrange the terms of Equation S8:

$$\underbrace{\left(-\frac{\partial pCO_{2w}}{\partial DIC} DIC_{FCO_2}\right)}_{Flux\ response} + \underbrace{(\partial_t pCO_{2w})}_{pCO_2\ change}$$

$$\approx \underbrace{\left(\frac{\partial pCO_{2w}}{\partial DIC} DIC_H + \frac{\partial pCO_{2w}}{\partial Alk} Alk_H + \frac{\partial pCO_{2w}}{\partial S} S_H\right)}_{H_{Circ}}$$

$$+ \underbrace{\left(\frac{\partial pCO_{2w}}{\partial DIC} DIC_V + \frac{\partial pCO_{2w}}{\partial Alk} Alk_V + \frac{\partial pCO_{2w}}{\partial S} S_V\right)}_{V_{Circ}}$$

$$+ \underbrace{\left(\frac{\partial pCO_{2w}}{\partial DIC} DIC_{FW} + \frac{\partial pCO_{2w}}{\partial Alk} Alk_{FW} + \frac{\partial pCO_{2w}}{\partial S} S_{FW}\right)}_{FW}$$

$$+ \underbrace{\left(\frac{\partial pCO_{2w}}{\partial DIC} DIC_{Bio} + \frac{\partial pCO_{2w}}{\partial Alk} Alk_{Bio}\right)}_{Bio}$$

$$+ \underbrace{\left(\frac{\partial pCO_{2w}}{\partial T} T_H + \frac{\partial pCO_{2w}}{\partial T} T_V + \frac{\partial pCO_{2w}}{\partial T} T_Q\right)}_{Thermal} \tag{S9}$$

The change of pCO_2 with time (*pCO_2 change*) and the response of carbon flux at the sea-air to the ocean pCO_2 (*Flux response*) on the left-hand side (LHS) can be influenced by five main categories on the right-hand side (RHS). They are the horizontal and vertical transports of dissolved species, that is, DIC, Alk, and salinity (H_{circ} and V_{circ}), the dilution/concentration effects induced by fresh-water fluxes and evaporation (*FW*), the biological effects due to photosynthesis, respiration, calcium carbonate dissolution/precipitation, denitrification, and nitrification (*Bio*), and vertical and horizontal transports and air-sea flux of heat (*Thermal*). The change in sea-air carbon flux can be analyzed more comprehensively by this method (Liao et al., 2020).

The coefficients required by the above Equation refer to the following Equation, where the overbar denotes 1990-2021 annual means (Liao et al., 2020; Lovenduski et al., 2007; Sarmiento et al., 2007):

$$\frac{\partial pCO_{2w}}{\partial DIC} \approx \frac{\overline{pCO_{2w}}}{\overline{DIC}} \frac{3\times\overline{Alk}\times\overline{DIC}-2\times\overline{DIC}^2}{(2\times\overline{DIC}-\overline{Alk})(\overline{Alk}-\overline{DIC})} \tag{S10}$$

$$\frac{\partial pCO_{2w}}{\partial Alk} \approx -\frac{\overline{pCO_{2w}}}{\overline{Alk}} \frac{\overline{Alk}^2}{(2\times\overline{DIC}-\overline{Alk})(\overline{Alk}-\overline{DIC})} \tag{S11}$$

$$\frac{\partial pCO_{2w}}{\partial T} \approx \overline{pCO_{2w}} \times 0.0423 \tag{S12}$$

$$\frac{\partial pCO_{2w}}{\partial S} \approx \frac{\overline{pCO_{2w}}}{\bar{S}} \tag{S13}$$

The coefficients of DIC, T, and S are positive, so pCO_{2w} increases with their increase. Similarly, the coefficient of ALK is negative, so pCO_{2w} decreases with the increase of ALK. DIC and ALK have opposite effects on the change of pCO_{2w}. Studies have shown that DIC usually plays a dominant role in influencing the change of pCO_{2w} because the coefficient of DIC is larger than that of ALK (Doney et al., 2009; Le Quéré et al., 2000; Takahashi et al., 2003). However, in some special cases, when affected by abnormal precipitation, ALK will overcome the influence of DIC to control the change of pCO_{2w} (Liao et al., 2020).

Section S4 Selection of La Niña and El Niño events

We define La Niña and El Niño as 5 consecutive overlapping 3-month periods at or above the +1.0℃ anomaly for warm (El Niño) events and at or below the +1.0℃ anomaly for cool (La Niña) events (https://ggweather.com/enso/oni.htm). La Niña events include the following six: 1995-1996, 1998-1999, 1999-2000, 2007-2008, 2010-2011, 2011-2012. El Niño events include the following six: 1991-1992, 1994-1995, 1997-1998, 2002-2003, 2009-2010, 2015-2016. Unless otherwise stated in the following, the observed and simulated responses and control mechanisms during La Niña and El Niño are the composite mean results of corresponding events. The year 1 is used to represent the first year during La Niña and El Niño events, year 2 is used to represent the following year, and year 3 denotes the third year.

Section S5 Ocean carbon responses to EP and CP El Niños

Of the six El Niño events we selected, where CP El Niño events are 1991-1992, 1994-1995, 2002-2003, 2009-2010; EP El Niño events are 1997-1998, 2015-2016 (Ren & Jin, 2011; Wang et al., 2022; Yu et al., 2012). The composited mean of these El Niño events is shown in Figures S14-S16. The air-sea carbon flux anomalies (Figure S14) caused by EP El Niño extend along the equator from the western equatorial Pacific Ocean to the eastern equatorial Pacific Ocean with a larger amplitude (more than -10 $gC/m^2/yr$). During CP El Niño, the air-sea carbon flux anomalies only locate in the western and central Pacific Ocean with a weak amplitude (about -6 $gC/m^2/yr$). The temporal evolution of ocean pCO_2 anomalies (Figure S15) indicates that EP El Niño drives a long duration of ocean pCO_2 response while CP Niño drives a short duration. And EP El Niño is often followed by La Nina.

The spatial and temporal response differences are closely related to the vertical transport, fresh-water flux, and horizontal transport terms between EP El Niño and CP El Niños (Figure S16). The vertical transport term reduces ocean pCO_2 due to a weakened upwelling during El Niño and the fresh-water flux term also reduces ocean pCO_2 through a dilution effect for more precipitation during El Niño. These two terms determine the equatorial ocean pCO_2 anomaly. The horizontal transport term (poleward Ekman transport) controls the poleward extension of ocean pCO_2 anomaly from the equator to the middle latitude. As shown in Figure S16, the strong vertical transport (upwelling/mixing) (-10 μatm/month) and fresh-water flux (precipitation/evaporation) (-10 μatm/month) terms extend along the equator in the whole equatorial Pacific Ocean during EP El Niño. In the CP El Niño, the strong vertical transport (-8 μatm/month) and the fresh-water flux (-6 μatm/month) terms only distribute in the western and central Pacific Ocean. Vertical transport and fresh-water flux are two dominant terms that drive the eastward extension of ocean pCO_2 anomaly. This is probably the reason that the ocean pCO_2 response to EP El Niño is observed in the whole equatorial Pacific Ocean and the ocean pCO_2 anomaly is only observed in the western and central Pacific Ocean during CP El Niño. The horizontal transport term is much stronger during EP El Niño (-10 μatm/month) than CP El Niño (-6 μatm/month) which explains the strong poleward extension and weak poleward extension. The discussion is apparently not enough due to word limitation, more detailed discussions are needed in future separate research.

Section S6 Ocean carbon budget imbalance

The net air-sea CO_2 flux anomaly is estimated using the simulations A and C in the global carbon budget projects led by Pierre Friedlingstein (Friedlingstein et al., 2022). The simulation A is driven by interannual forcing and interannual atmospheric CO_2, while the simulation C is driven by climatological forcing and interannual atmospheric CO_2. The difference between simulations A and C is considered as net air-sea CO_2 flux anomaly driven by ENSO and other natural climate variability. A positive flux indicates a weakened ocean carbon sink due to natural climate variability. The net air-sea CO_2 flux anomaly in the tropical Pacific Ocean and other ocean basins is summarized in Table S1 which helps to understand the separated regional impacts on the ocean carbon budget imbalance from 1990 to 2021. The largest contribution is from the Pacific Ocean and Indian Ocean which might be closely related to ENSO, Pacific Decadal Oscillation (PDO), and Indian Ocean Dipole (IOD) signals. Further research is needed in discussing the contribution of these interannual/decadal signals and other signals like Southern Annual Mode (SAM) between ocean basins to the global imbalance.

Table S1. Overall air-sea carbon flux in different regions from 1990 to 2021 (unit: PgC)

Regions	Tropical Pacific Ocean	North Pacific Ocean	South Pacific Ocean	Indian Ocean	Atlantic Ocean	Arctic Ocean	Southern Ocean	Global Ocean
Flux	0.71	0.19	1.15	0.88	0.42	0.00	0.83	3.49

*The Tropical Pacific Ocean is defined as 150°E-285°E, 15°S-15°N; the North and South Pacific Ocean is the region to the north of 15°N and to the south of 15°S respectively. A positive value indicates a weakened ocean carbon sink due to natural climate variability like ENSO.

Section S7 Figure S1-S16

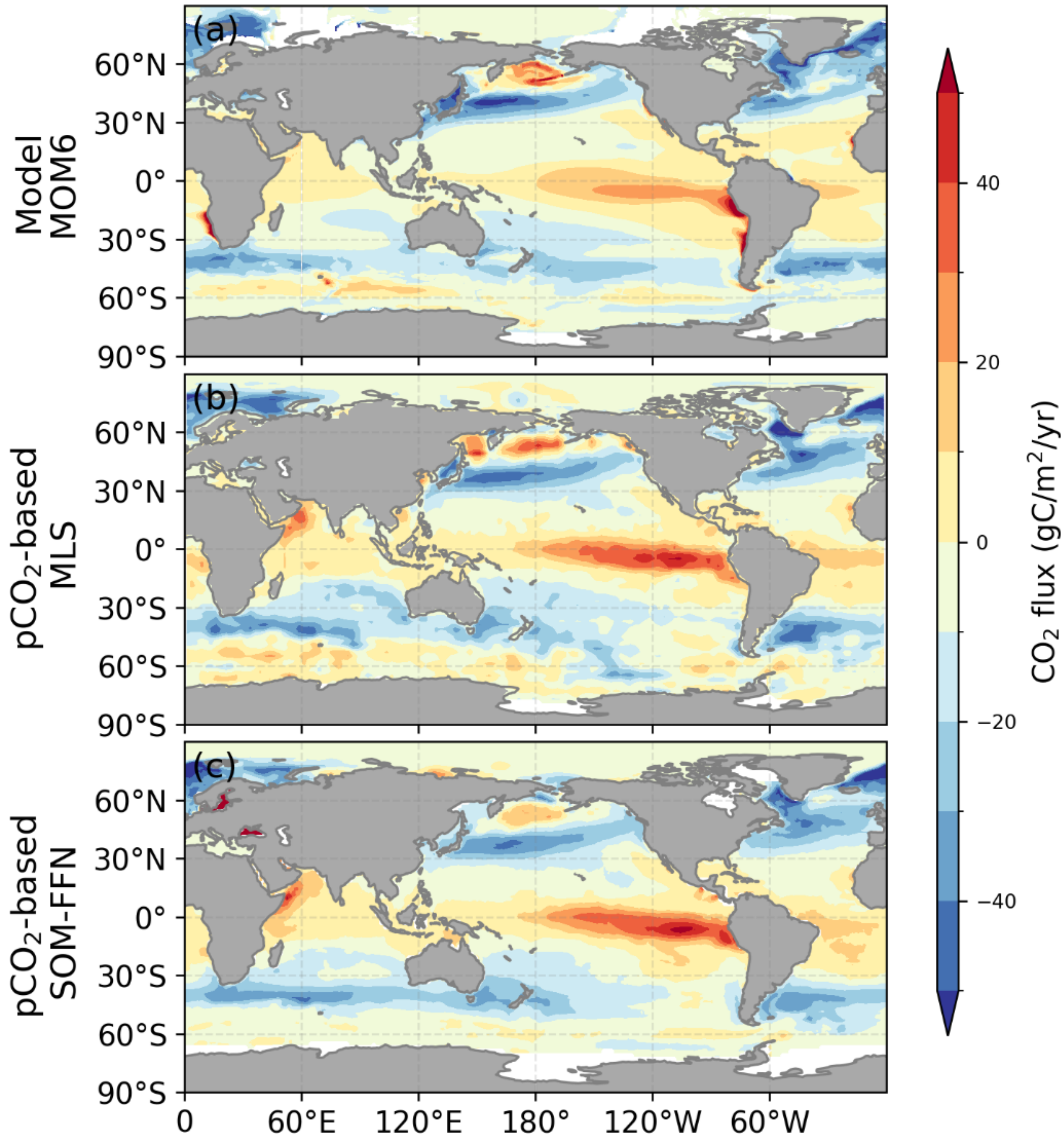

Figure S1. Spatial map comparisons of climatological mean of air-sea CO_2 fluxes (a-c). A positive flux denotes an outgassing from the ocean to atmosphere. Observational pCO_2-based products are from Rödenbeck et al. (2013) for MLS and Landschützer et al. (2014) for SOM-FFN.

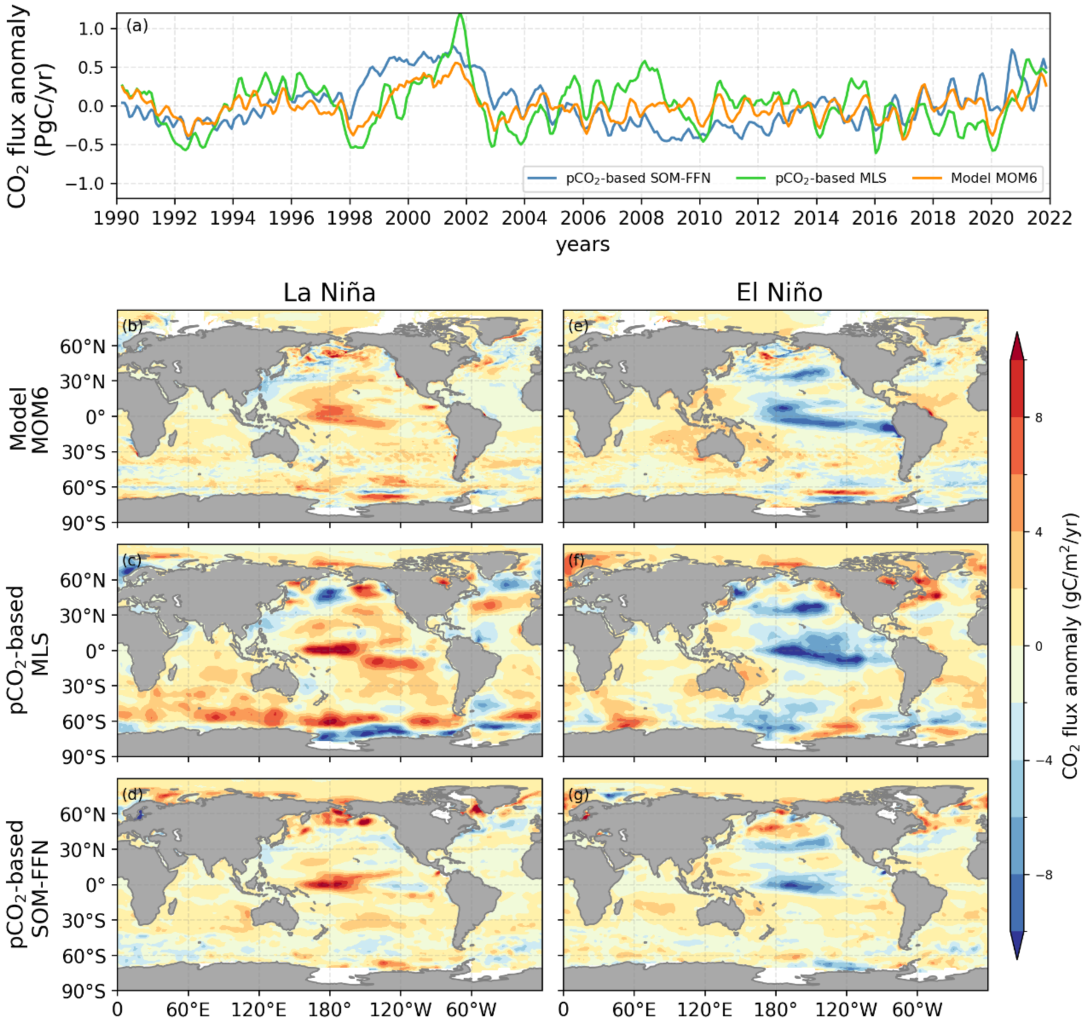

Figure S2. Time-series of (a) air-sea CO_2 flux anomaly over global ocean, and spatial distribution of air-sea CO_2 flux anomaly between La Niña (b-d) and El Niño (e-g) in two pCO_2-based data products and the ocean model MOM6-COBALT2. The spatial distribution is six-month mean (January of year 2 to June of year 2) for a composite of six La Niña events and six El Niño events. Positive values suggest an outgassing from ocean to atmosphere, indicating amplified outgassing by the ocean. Observational pCO_2-based products are from Rödenbeck et al. (2013) for MLS and Landschützer et al. (2014) for SOM-FFN.

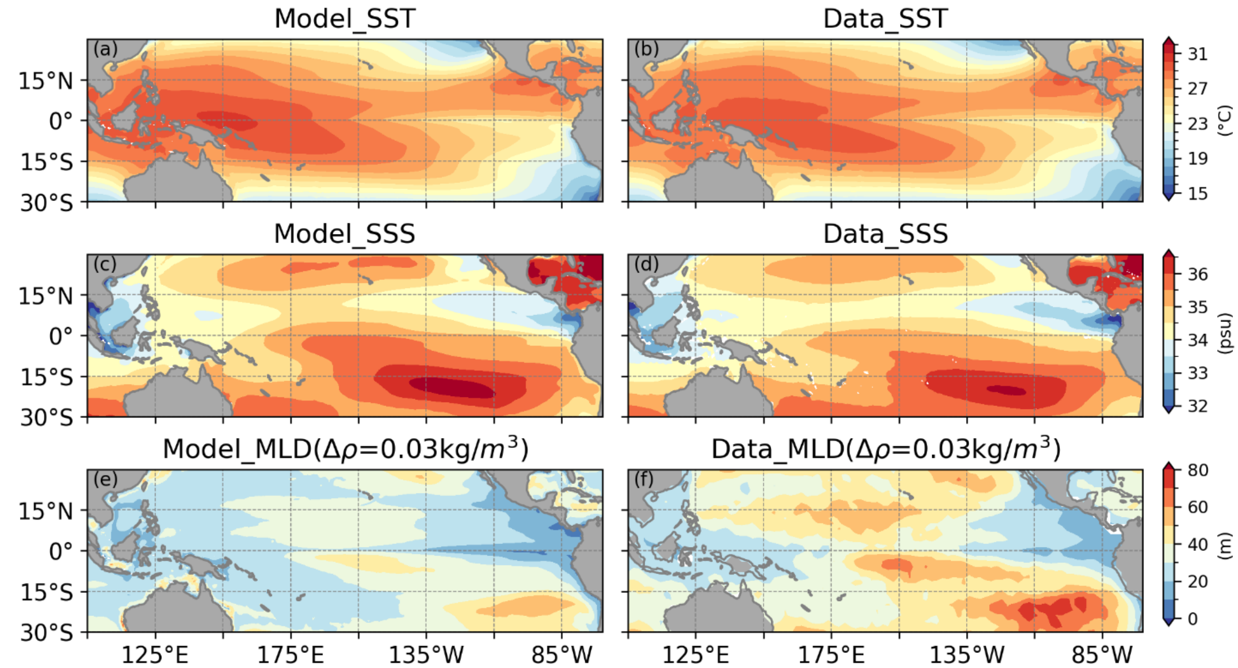

Figure S3. Spatial map comparisons about climatological mean of temperature (unit: °C), salinity (unit: psu), and mixed layer depth (unit: m), where (a, c, e) are from the MOM6-COBALT2 model, (b) is from OISST v2, (d) is from OISSS v1, and (f) is from de Boyer Montégut et al., (2004).

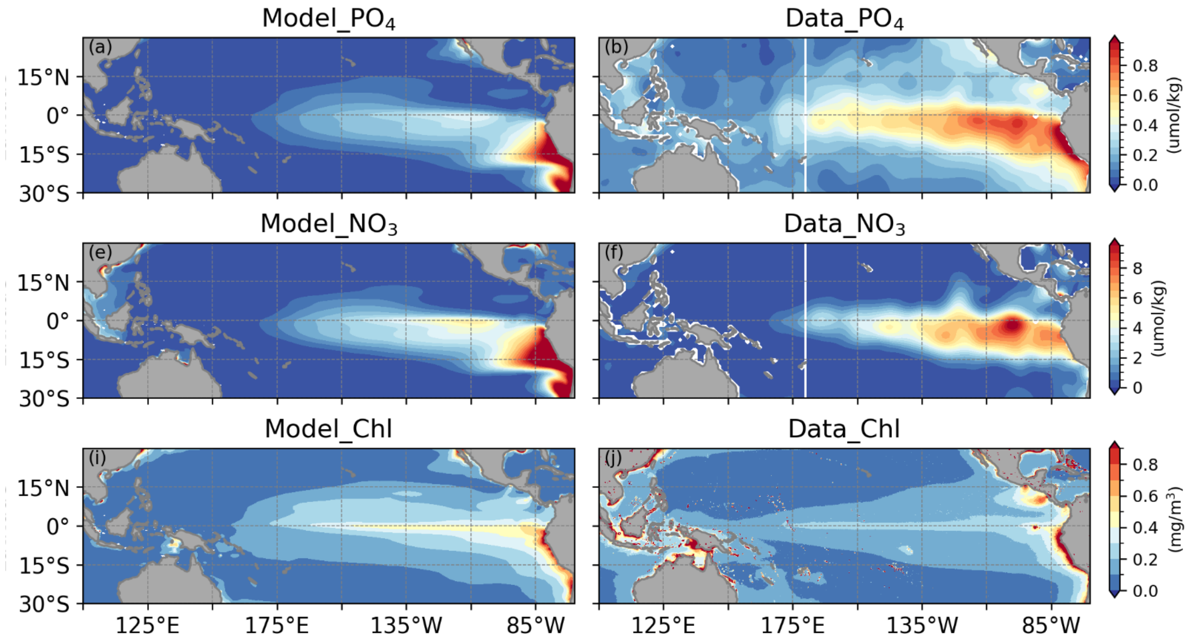

Figure S4. Spatial map comparisons of climatological mean of PO_4 (unit: µmol/kg), NO_3 (unit: µmol/kg), and chlorophyll (unit: mg/m^3), where (a, c, e) are from the MOM6-COBALT2 model, (b, d) are from World Ocean Atlas 2013, and (f) is from GlobColour satellite data.

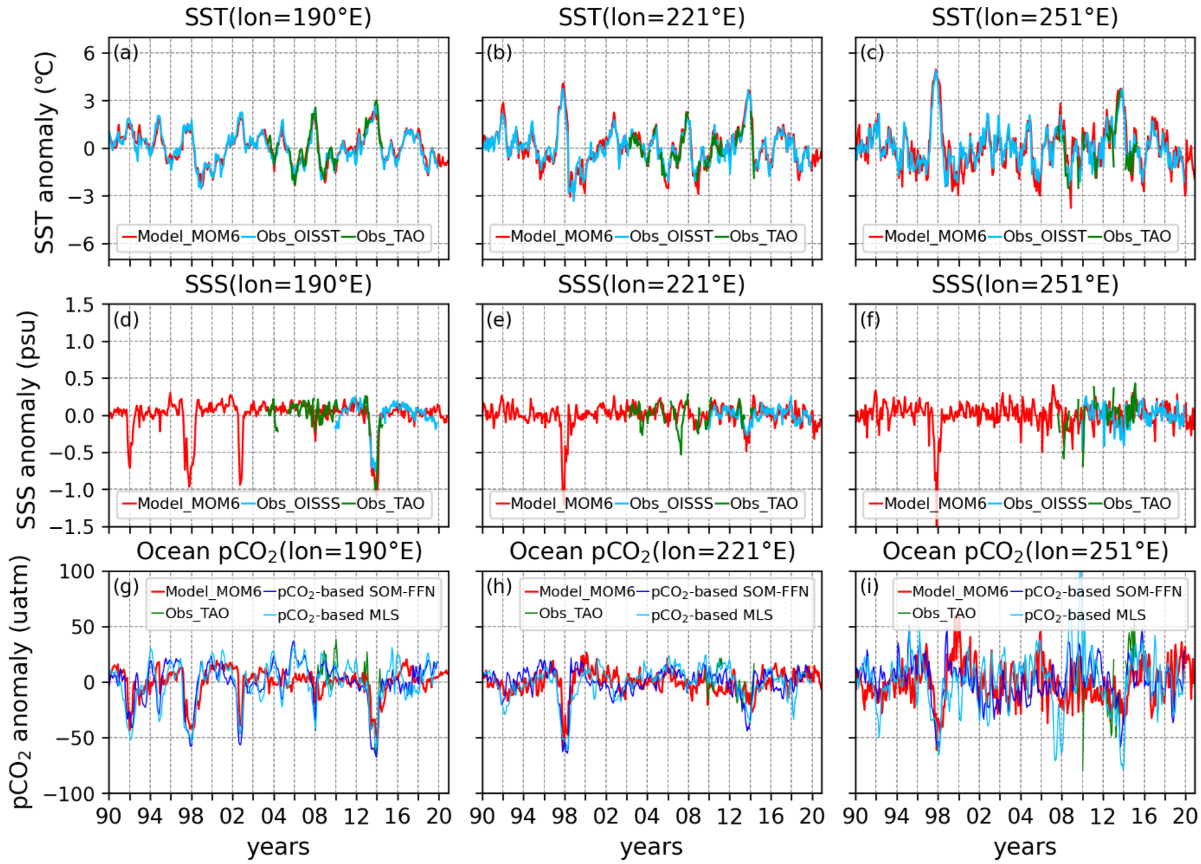

Figure S5. Time series comparison of temperature anomaly (unit: °C), salinity anomaly (unit: psu), and ocean pCO_2 anomaly (unit: μatm) at three TAO moorings (190°E, 221°E, 251°E) along the equator. The results are averaged in the 1×1° box over the three TAO moorings from the MOM6-COBALT2, pCO_2-based SOM-FFN product (Landschützer et al., 2014), and pCO_2-based MLS product (Rödenbeck et al., 2013).

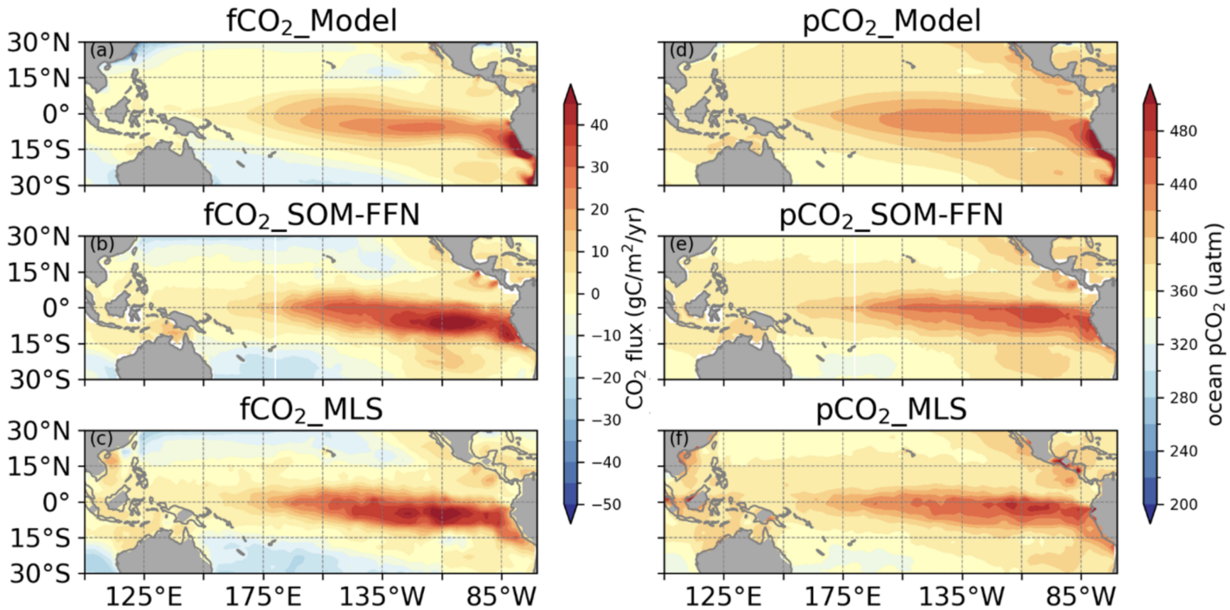

Figure S6. Spatial map comparisons of climatological mean of air-sea CO_2 fluxes (a-c) and ocean pCO_2 (d-f). Observed CO_2 flux and ocean pCO_2 are from pCO_2-based SOM-FFN and MLS data products. A positive flux denotes an outgassing from the ocean to atmosphere.

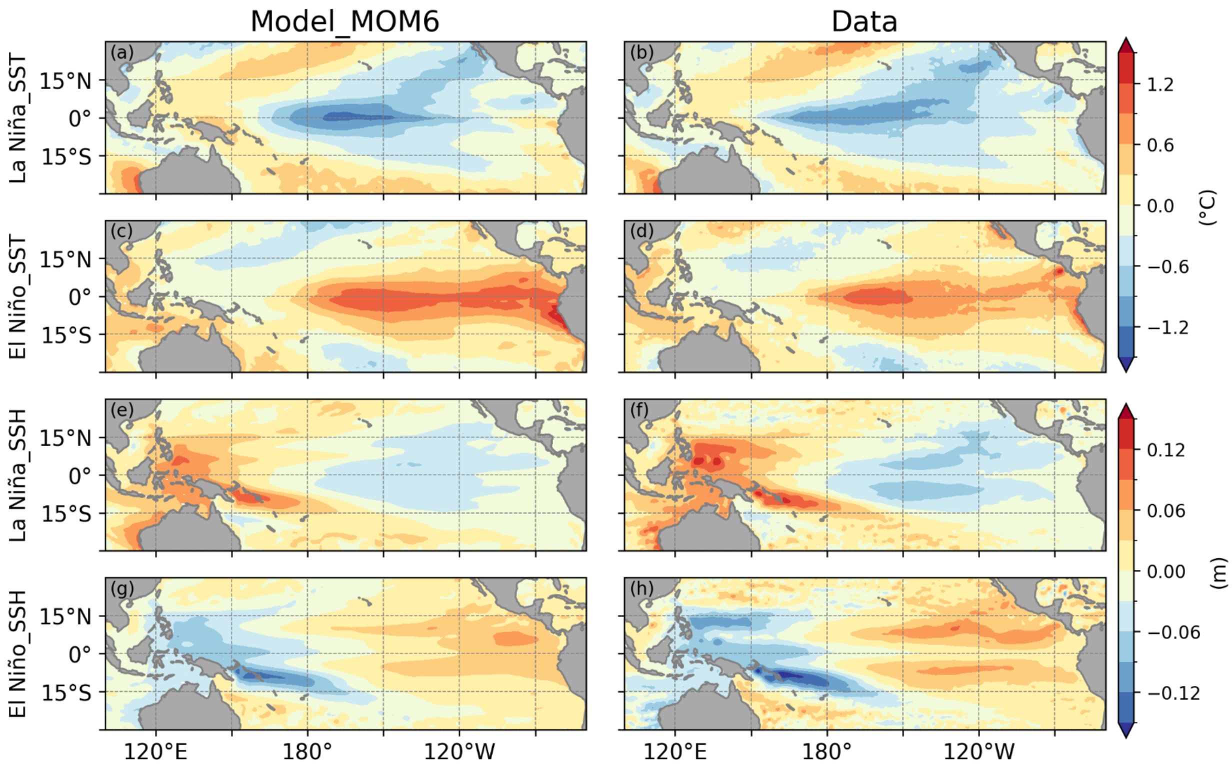

Figure S7. Spatial map comparisons of sea surface temperature anomaly (a-d, unit: °C), sea surface height anomaly (e-h, unit: m) during La Niña (a-b, e-f, i) and El Niño (c-d, g-h, j). The SST data is from OISST v2, and SSH data is from AVISO. Composite La Niña and El Niño events are defined in Section S4.

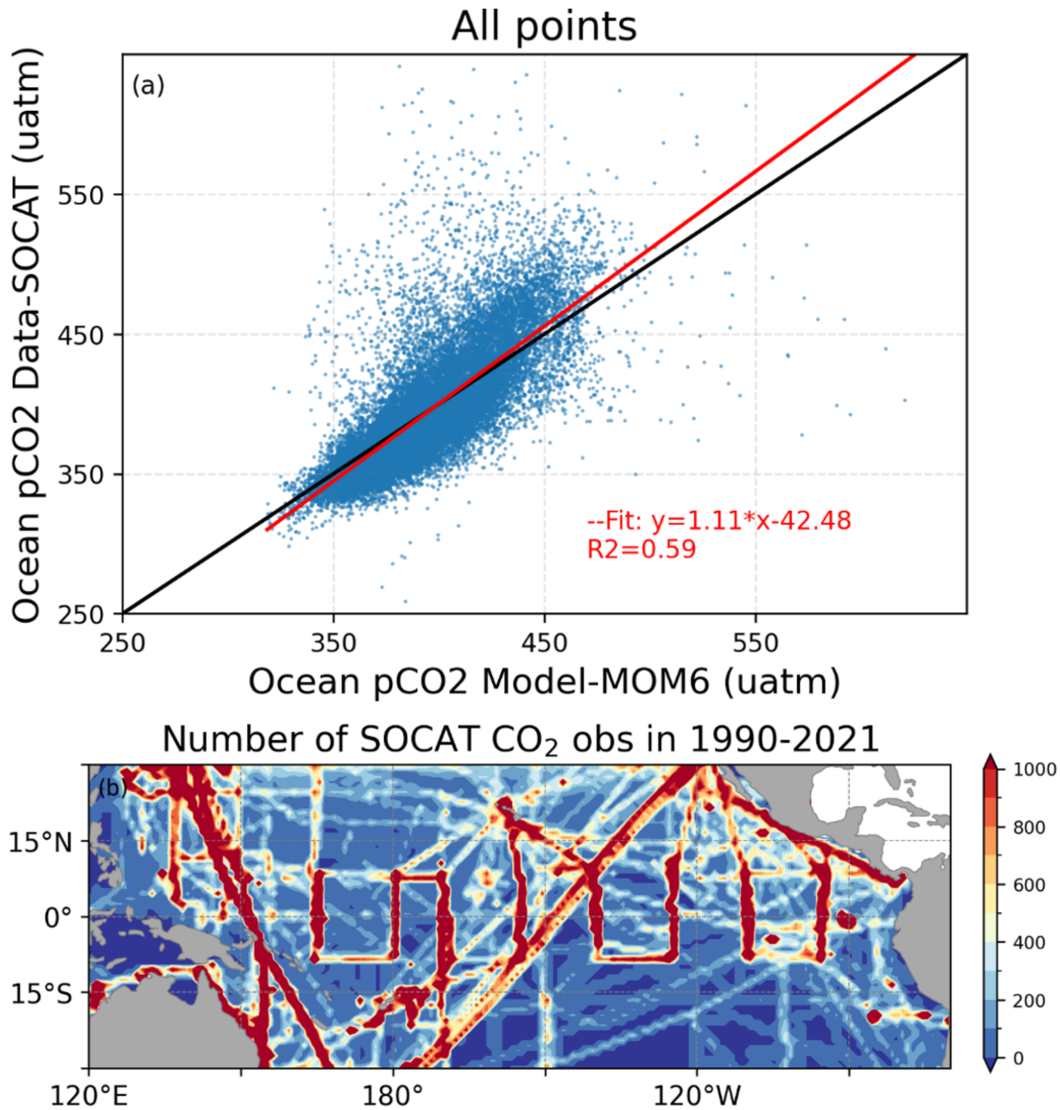

Figure S8. Comparison of observed and simulated ocean pCO_2 (a) in the tropical Pacific Ocean (150ºE-285ºE, 15ºS-15ºN) during 1990-2021. The observed ocean pCO_2 is collected from SOCAT monthly database. The simulated ocean pCO_2 is interpolated to match the SOCAT observation locations and times. The black line is the 1-to-1 line and the red line is regression line between data and model. (b) is the number of SOCAT CO_2 observations per degree from 1990 to 2021.

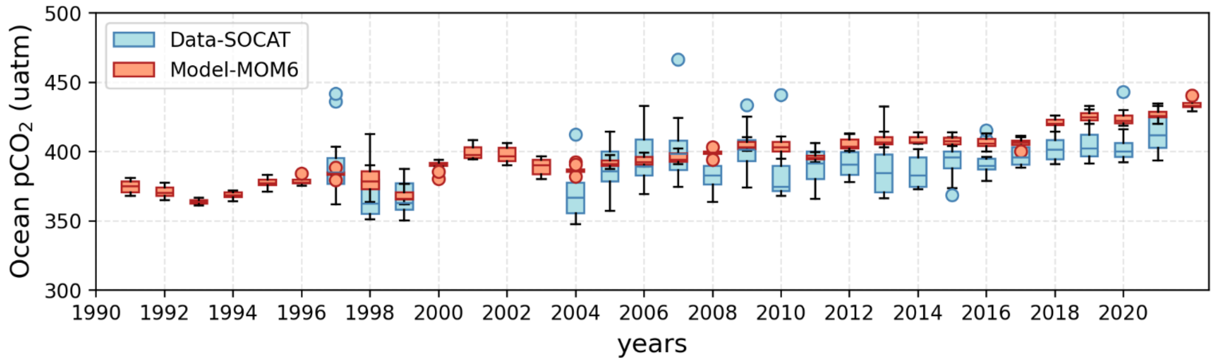

Figure S9. The year-by-year box plot comparison of observed and simulated ocean pCO_2 in the tropical Pacific Ocean (150ºE-285ºE, 15ºS-15ºN) during 1990-2021. The observed ocean pCO_2 is collected from SOCAT monthly database. The simulated ocean pCO_2 is interpolated to match the SOCAT observational locations and times.

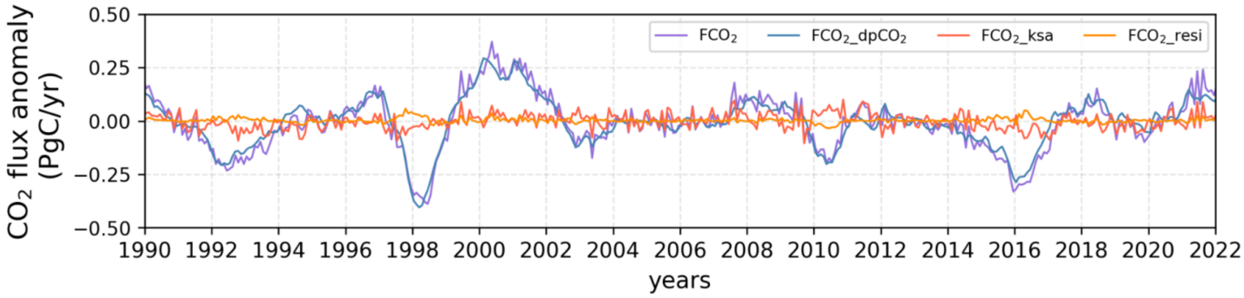

Figure S10. Time series of decompositions of simulated air–sea CO_2 flux anomaly from 1990 to 2021 in the tropical Pacific Ocean. A positive flux denotes an anomalous outgassing from the ocean to atmosphere. The decomposition is based on Equation S1.

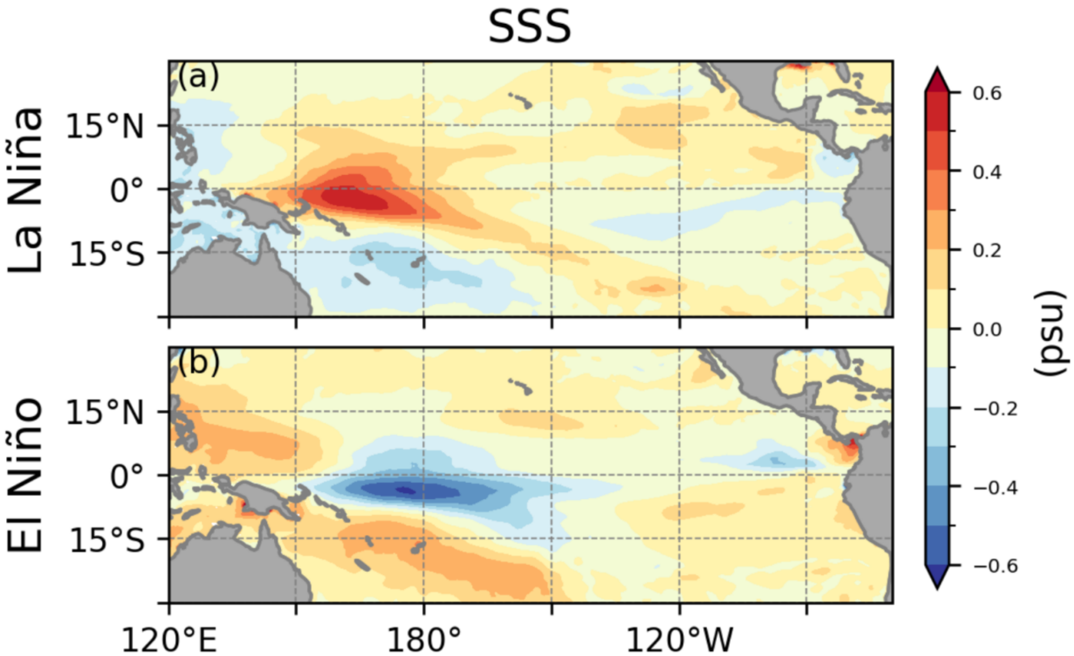

Figure S11. Composite mean sea surface salinity anomaly in the tropical Pacific Ocean during La Niña (a) and El Niño (b). Composite La Niña and El Niño events are defined in Section S4.

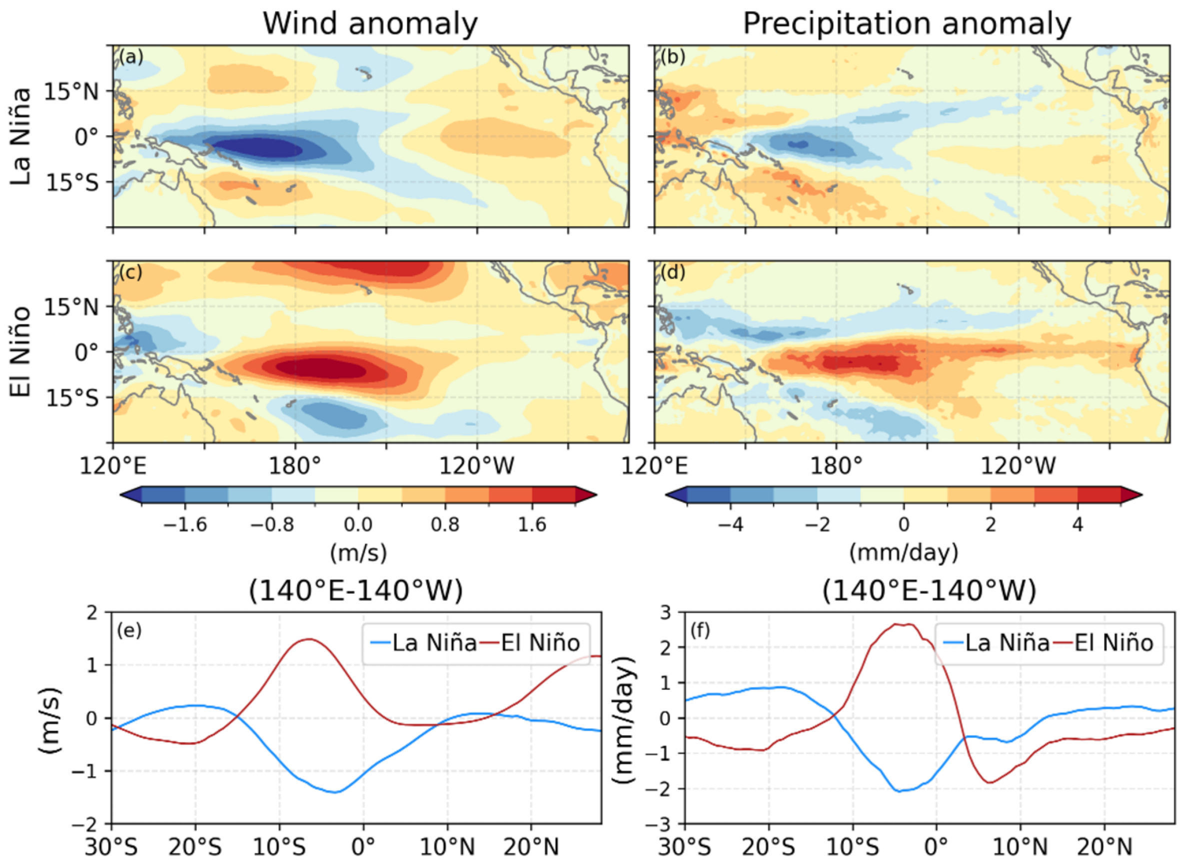

Figure S12. Composite mean wind anomaly (a, c, unit: m/s) and precipitation anomaly (b,d, unit: mm/day) in the tropical Pacific Ocean during La Niña (a-b) and El Niño (c-d). Composite mean wind (e) and precipitation (f) anomalies along the latitude averaged in the 140°E-140°W during La Niña and El Niño. Composite La Niña and El Niño events are defined in Section S4. Positive wind anomaly indicates the direction from west to east.

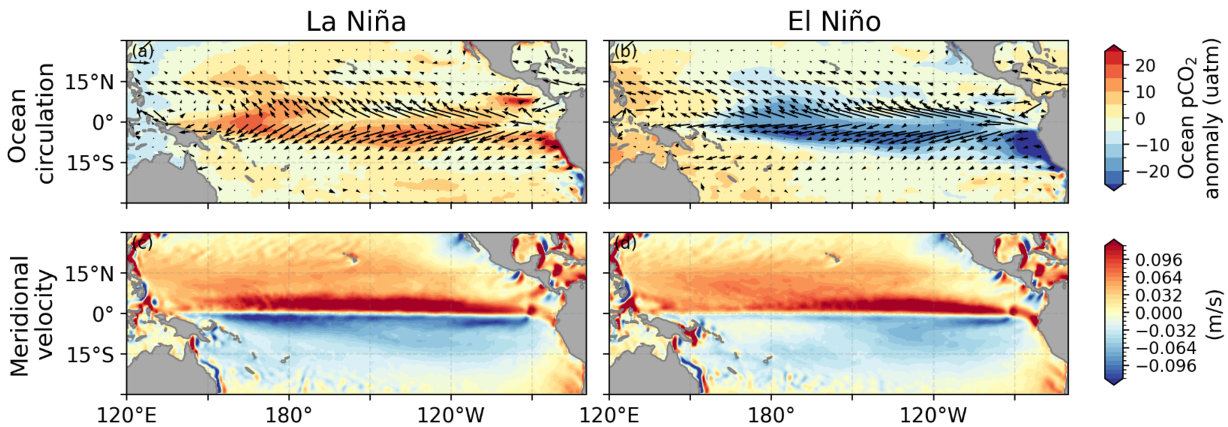

Figure S13. Ocean circulation vector in the tropical Pacific Ocean during La Niña (a) and El Niño (b), and spatial maps of meridional velocity in the tropical Pacific Ocean during La Niña (c) and El Niño (d). Positive meridional velocity indicates the direction from south to north.

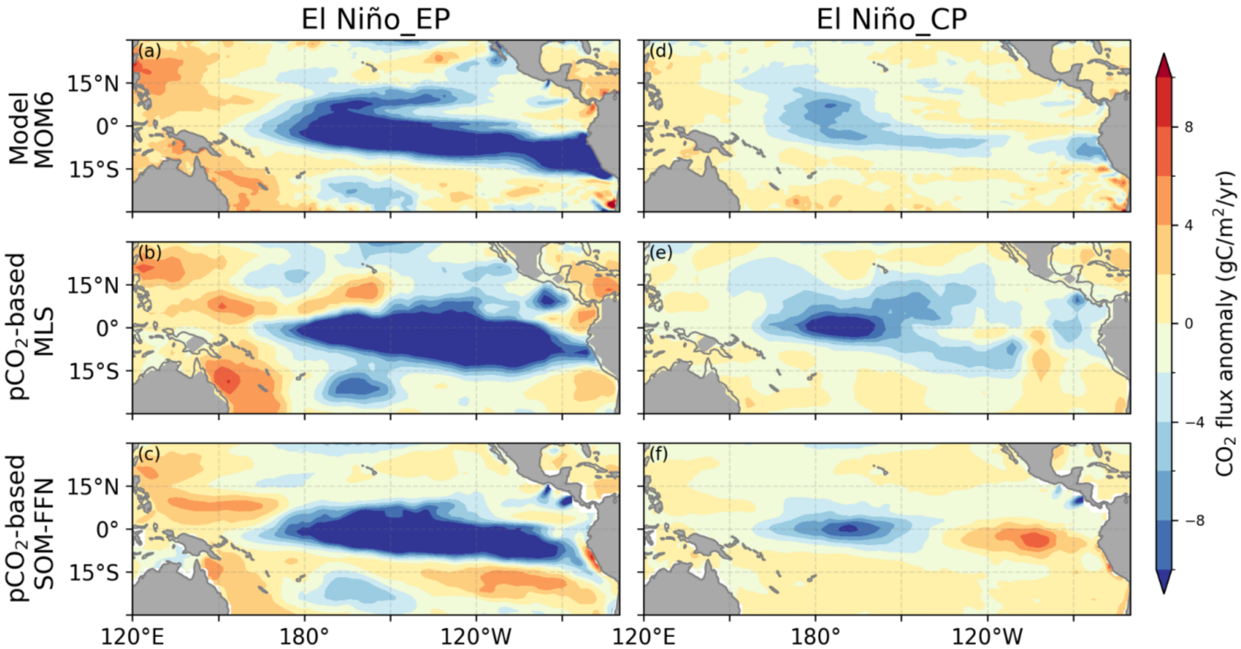

Figure S14. Spatial distribution of air-sea CO_2 flux anomaly between EP El Niño (a-c) and CP El Niño (d-f) in two pCO_2-based data products and the ocean model MOM6-COBALT2. The spatial distribution is six-month mean (January of year 2 to June of year 2) for a composite of two EP El Niño events and four CP El Niño events. Observational pCO_2-based products are from Rödenbeck et al. (2013) for MLS and Landschützer et al. (2014) for SOM-FFN.

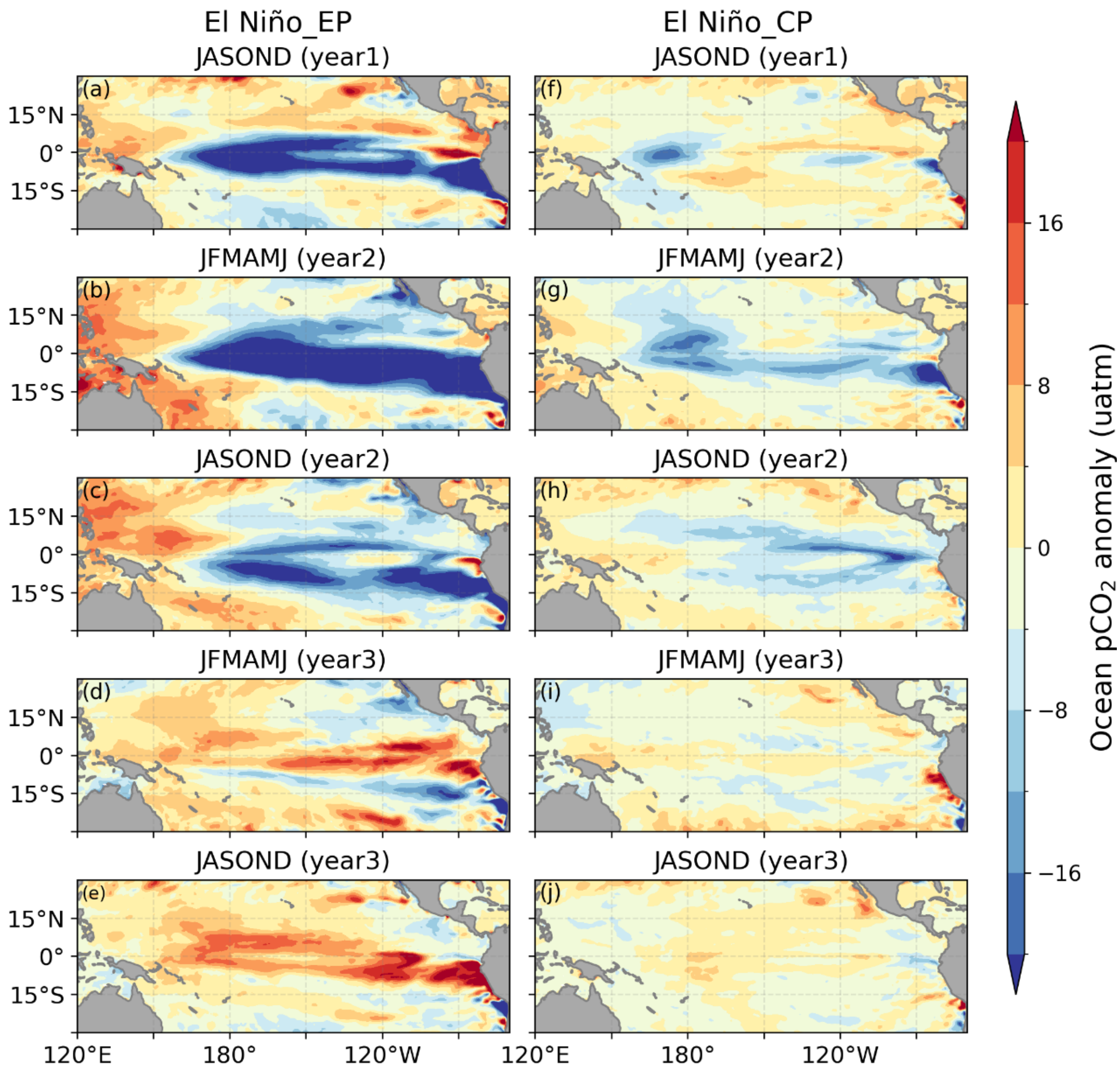

Figure S15. The evolution of ocean pCO_2 anomaly during EP El Niño (a-e) and CP El Niño (f-j) from July of year 1 to December of year 3 based on the MOM6-COBALT2 model result. JASOND (year1) indicates the months from July to December in the first year and JFMAMJ (year2) indicates the months from January to June in the second year. ENSO peaks in January and February of year 2. The results are averaged over six months for a composite of two EP El Niño events and four CP El Niño events. Positive values are anomalous increase of ocean pCO_2.

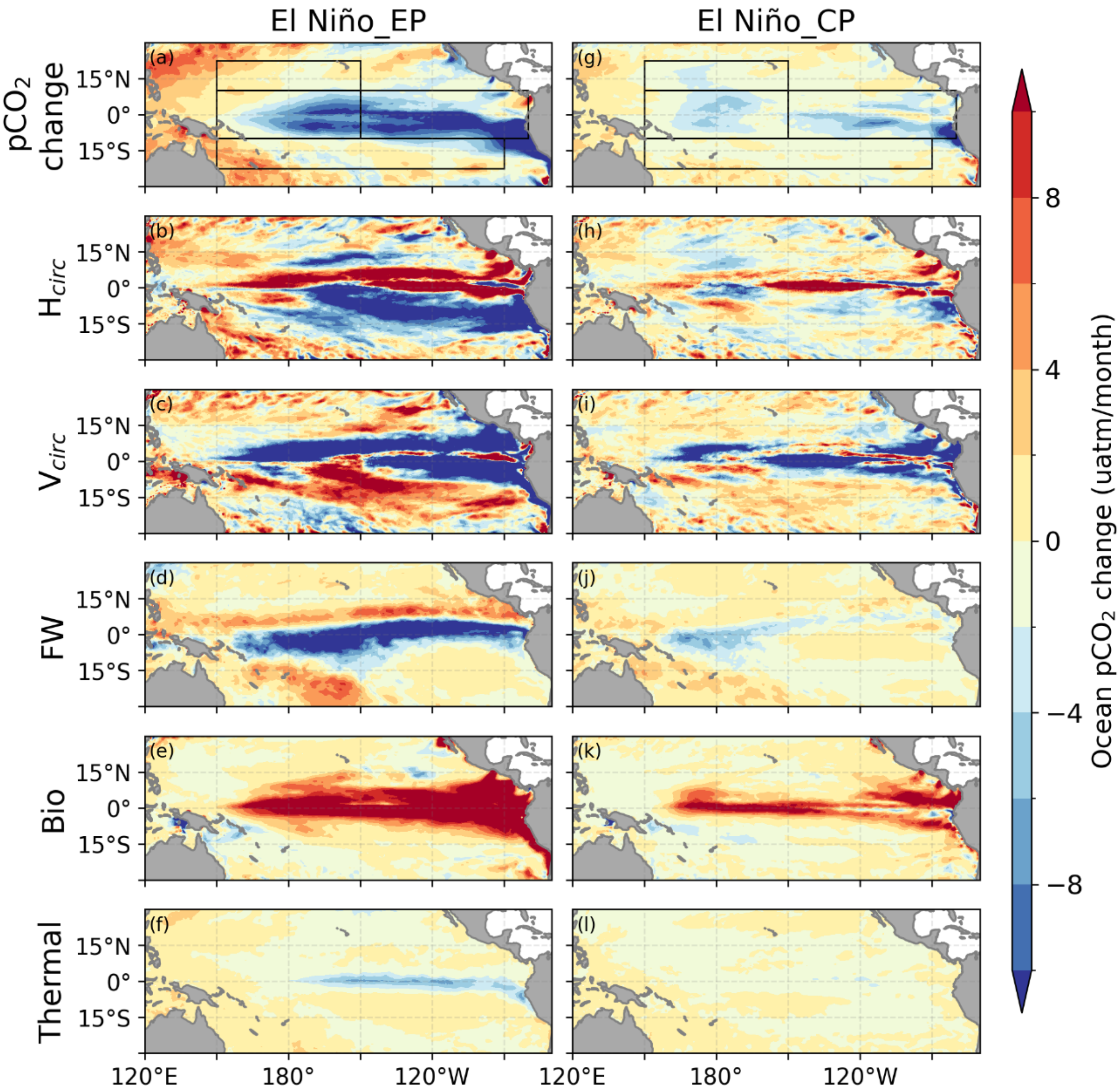

Figure S16. Processes controlling the composite carbon responses to EP El Niño (a-f) and CP El Niño (g-l) in the model between July of year 1 and June of year 2 based on Equation 2. The pCO_2 change (a, g), which includes pCO_2 time tendency and changes by the air-sea flux, can be attributed to changes in horizontal (b, h) and vertical (c, i) transports, fresh-water fluxes (d, j), biological activities (e, k), and thermal changes (f, l) (a = b + c + d + e + f, g = h + i + j + k + l, see Equation 2).

References

Banzon, V., Smith, T. M., Chin, T. M., Liu, C., & Hankins, W. (2016). A long-term record of blended satellite and in situ sea-surface temperature for climate monitoring, modeling and environmental studies. *Earth Syst. Sci. Data*, *8*(1), 165-176. https://doi.org/10.5194/essd-8-165-2016

de Boyer Montégut, C., Madec, G., Fischer, A. S., Lazar, A., & Iudicone, D. (2004). Mixed layer depth over the global ocean: An examination of profile data and a profile-based climatology. *Journal of Geophysical Research: Oceans*, *109*(C12), 11-12. https://doi.org/10.1029/2004JC002378

Doney, S. C., Lima, I., Feely, R. A., Glover, D. M., Lindsay, K., Mahowald, N., et al. (2009). Mechanisms governing interannual variability in upper-ocean inorganic carbon system and air–sea CO_2 fluxes: Physical climate and atmospheric dust. *Deep Sea Research Part II: Topical Studies in Oceanography*, *56*(8), 640-655. https://doi.org/10.1016/j.dsr2.2008.12.006

Friedlingstein, P., O'Sullivan, M., Jones, M. W., Andrew, R. M., Gregor, L., Hauck, J., et al. (2022). Global carbon budget 2022. *Earth Syst. Sci. Data*, *14*(11), 4811-4900. https://doi.org/10.5194/essd-14-4811-2022

Garcia, H. E., Boyer, T. P., Locarnini, R. A., Antonov, J. I., Mishonov, A. V., Baranova, O. K., et al. (2013). World ocean atlas 2013. Volume 3, Dissolved oxygen, apparent oxygen utilization, and oxygen saturation [Atlas]. *3*. https://doi.org/10.7289/V5XG9P2W (NOAA atlas NESDIS ; 75)

Garcia, H. E., Locarnini, R. A., Boyer, T. P., Antonov, J. I., Baranova, O. K., Zweng, M. M., et al. (2013). World ocean atlas 2013. Volume 4, Dissolved inorganic nutrients (phosphate, nitrate, silicate) [Atlas]. https://doi.org/10.7289/V5J67DWD (NOAA atlas NESDIS ; 76)

Khatiwala, S., Tanhua, T., Mikaloff Fletcher, S., Gerber, M., Doney, S. C., Graven, H. D., et al. (2013). Global ocean storage of anthropogenic carbon. *Biogeosciences*, *10*(4), 2169-2191. https://doi.org/10.5194/bg-10-2169-2013

Landschützer, P., Gruber, N., Bakker, D. C. E., & Schuster, U. (2014). Recent variability of the global ocean carbon sink. *Global Biogeochemical Cycles*, *28*(9), 927-949. https://doi.org/10.1002/2014GB004853

Le Quéré, C., Orr, J. C., Monfray, P., Aumont, O., & Madec, G. (2000). Interannual variability of the oceanic sink of CO_2 from 1979 through 1997. *Global Biogeochemical Cycles*, *14*(4), 1247-1265. https://doi.org/10.1029/1999GB900049

Liao, E., Lu, W., Xue, L., & Du, Y. (2024). Weakening Indian Ocean carbon uptake in 2015: The role of amplified basin-wide warming and reduced Indonesian throughflow. *Limnology and Oceanography Letters*, *9*(4), 442-451. https://doi.org/10.1002/lol2.10397

Liao, E., Resplandy, L., Liu, J., & Bowman, K. W. (2020). Amplification of the ocean carbon sink during El Niños: Role of poleward Ekman transport and influence on atmospheric CO_2. *Global Biogeochemical Cycles*, *34*(9), e2020GB006574. https://doi.org/10.1029/2020GB006574

Locarnini, R. A., Mishonov, A. V., Antonov, J. I., Boyer, T. P., Garcia, H. E., Baranova, O. K., et al. (2013). World ocean atlas 2013. Volume 1, Temperature [Atlas]. https://doi.org/10.7289/V55X26VD (NOAA atlas NESDIS ; 73)

Lovenduski, N. S., Gruber, N., Doney, S. C., & Lima, I. D. (2007). Enhanced CO_2 outgassing in the Southern Ocean from a positive phase of the Southern Annular Mode. *Global Biogeochemical Cycles*, *21*(2), GB2026. https://doi.org/10.1029/2006GB002900

Maritorena, S., d'Andon, O. H. F., Mangin, A., & Siegel, D. A. (2010). Merged satellite ocean color data products using a bio-optical model: Characteristics, benefits and issues. *Remote Sensing of Environment*, *114*(8), 1791-1804. https://doi.org/10.1016/j.rse.2010.04.002

McPhaden, M. J., Busalacchi, A. J., Cheney, R., Donguy, J.-R., Gage, K. S., Halpern, D., et al. (1998). The Tropical Ocean-Global Atmosphere observing system: A decade of progress. *Journal of Geophysical Research: Oceans*, *103*(C7), 14169-14240. https://doi.org/10.1029/97JC02906

Melnichenko, O., P. Hacker, J. Potemra, T. Meissner, & Wentz, F. (2021). Aquarius/SMAP sea surface salinity optimum interpolation analysis. *IPRC Technical Note No, 7.* https://iprc.soest.hawaii.edu/users/oleg/oisss/GLB/OISSS_Product_Notes.pdf

Olsen, A., Key, R. M., van Heuven, S., Lauvset, S. K., Velo, A., Lin, X., et al. (2016). The Global Ocean Data Analysis Project version 2 (GLODAPv2) – an internally consistent data product for the world ocean. *Earth Syst. Sci. Data*, *8*(2), 297-323. https://doi.org/10.5194/essd-8-297-2016

Rayner, N. A., Parker, D. E., Horton, E. B., Folland, C. K., Alexander, L. V., Rowell, D. P., et al. (2003). Global analyses of sea surface temperature, sea ice, and night marine air temperature since the late nineteenth century. *Journal of Geophysical Research: Atmospheres*, *108*(D14), 4407. https://doi.org/10.1029/2002JD002670

Ren, H.-L., & Jin, F.-F. (2011). Niño indices for two types of ENSO. *Geophysical Research Letters*, *38*(4). https://doi.org/10.1029/2010GL046031

Rödenbeck, C., Keeling, R. F., Bakker, D. C. E., Metzl, N., Olsen, A., Sabine, C., & Heimann, M. (2013). Global surface-ocean pCO_2 and sea–air CO_2 flux variability from an observation-driven ocean mixed-layer scheme. *Ocean Sci.*, *9*(2), 193-216. https://doi.org/10.5194/os-9-193-2013

Sarmiento, J., Gruber, N., & McElroy, M. (2007). Ocean biogeochemical dynamics. *Physics Today*, *60*(6), 65. https://doi.org/10.1063/1.2754608

Stock, C. A., Dunne, J. P., & John, J. G. (2014). Global-scale carbon and energy flows through the marine planktonic food web: An analysis with a coupled physical–biological model. *Progress in Oceanography*, *120*, 1-28. https://doi.org/10.1016/j.pocean.2013.07.001

Sutton, A. J., Sabine, C. L., Maenner-Jones, S., Lawrence-Slavas, N., Meinig, C., Feely, R. A., et al. (2014). A high-frequency atmospheric and seawater pCO_2 data set from 14 open-ocean sites using a moored autonomous system. *Earth Syst. Sci. Data*, *6*(2), 353-366. https://doi.org/10.5194/essd-6-353-2014

Takahashi, T., Olafsson, J., Goddard, J. G., Chipman, D. W., & Sutherland, S. C. (1993). Seasonal variation of CO_2 and nutrients in the high-latitude surface oceans: A comparative study. *Global Biogeochemical Cycles*, *7*(4), 843-878. https://doi.org/10.1029/93GB02263

Takahashi, T., Sutherland, S. C., Feely, R. A., & Cosca, C. E. (2003). Decadal variation of the surface water pCO_2 in the western and central equatorial Pacific. *Science*, *302*(5646), 852-856. https://doi.org/10.1126/science.1088570

Wang, C., Li, J., Liu, Q., Huete, A., Li, L., Dong, Y., & Zhao, J. (2022). Eastern-Pacific and Central-Pacific Types of ENSO Elicit Diverse Responses of Vegetation in the West Pacific Region. *Geophysical Research Letters*, *49*(3), e2021GL096666. https://doi.org/10.1029/2021GL096666

Wanninkhof, R. (2014). Relationship between wind speed and gas exchange over the ocean revisited. *Limnology and Oceanography: Methods*, *12*(6), 351-362. https://doi.org/10.4319/lom.2014.12.351

Weiss, R. F., & Price, B. A. (1980). Nitrous oxide solubility in water and seawater. *Marine Chemistry*, *8*(4), 347-359. https://doi.org/10.1016/0304-4203(80)90024-9

Yu, J.-Y., Zou, Y., Kim, S. T., & Lee, T. (2012). The changing impact of El Niño on US winter temperatures. *Geophysical Research Letters*, *39*(15). https://doi.org/10.1029/2012GL052483

Zweng, M. M., Reagan, J. R., Antonov, J. I., Locarnini, R. A., Mishonov, A. V., Boyer, T. P., et al. (2013). World ocean atlas 2013. Volume 2, Salinity [Atlas]. https://doi.org/10.7289/V5251G4D (NOAA atlas NESDIS ; 74)